



# Randomness of optical turbulence generated by Rayleigh–Bénard convection using intensity statistics

NATHANIEL A. FERLIC,<sup>1,\*</sup> SVETLANA AVRAMOV-ZAMUROVIC,<sup>2</sup> OWEN O'MALLEY,<sup>2</sup>  
THOMAS KELLY,<sup>2</sup> AND K. PETER JUDD<sup>3</sup>

<sup>1</sup>Naval Air Warfare Center Aircraft Division, 22347 Cedar Point Road, Patuxent River, Maryland 20670, USA

<sup>2</sup>Weapons, Robotics, and Control Engineering Department, United States Naval Academy, 597 McNair Rd. Hopper Hall, Annapolis, Maryland 21402, USA

<sup>3</sup>United States Naval Research Laboratory, 4555 Overlook Ave. SW, Washington, DC 20375, USA

\*nathaniel.a.ferlic.civ@us.navy.mil

Received 7 February 2024; revised 2 April 2024; accepted 3 April 2024; posted 5 April 2024; published 6 May 2024

The experimental study of optical turbulence proves difficult due to challenges in generating controllable conditions in a laboratory environment. Confined water tanks that produce Rayleigh–Bénard (RB) convection are one method to generate optical turbulence using a controllable temperature gradient. It is of utmost concern to quantify the properties of the optical turbulence generated for characterization of other optical applications such as imaging, sensing, or communications. In this experimental study a Gaussian beam is propagated through a RB water tank where two intensity measurements are made at the receiver's pupil and focal plane. The pupil and focal plane results include quantification of the intensity fluctuation distribution, scintillation distribution, and refractive index structure constant at various values of the temperature gradient. The angle of arrival fluctuations is also calculated at the focal plane to obtain a second estimate of  $C_n^2$ . The pupil plane estimate for  $C_n^2$  using scintillation index and focal plane angle of arrival fluctuations is compared to preliminary predictions of  $C_n^2$  as a function of RB temperature gradient showing  $C_n^2 \sim \Delta T^{4/3}$ . The outcomes of the study confirm that the RB process produces intensity fluctuations that follow gamma–gamma and log-normal probability density functions. Estimates of the refractive index structure constant  $C_n^2$  produce the same trends with different magnitudes when measured from the pupil and focal plane. © 2024 Optica Publishing Group

<https://doi.org/10.1364/JOSAA.520909>

## 1. INTRODUCTION

Laser-based applications in the atmosphere or ocean, such as imaging [1], free-space communications [2], sensing [3], or directed energy [4], are subject to random density changes of the fluid due to turbulence. These random density changes vary the medium's refractive index, which affects light propagation by creating fluctuations in the optical path length and, consequently, the optical phase. This effect is called optical turbulence due to the manifestation of phase variations resulting in constructive and destructive interference that lead to intensity scintillation, beam wander, beam spreading, and loss of temporal and spatial coherence [5]. These effects must be thoroughly understood to predict system performance since characterization of the system cannot be done without knowledge of the conditions in which it was tested.

Modeling, atmospheric or underwater, optical turbulence treats the environment as a stochastic process with several limiting assumptions that offer crucial insight into its behavior [6]. Outdoor experiments are the most significant method to

validate these fundamental models and assumptions; however, controllability and repeatability are difficult [7–9]. Laboratory reproduction of the outdoor randomness can be done by creating heated air or water chambers with limited volumes. These chambers can produce small turbulence scales at speeds comparable to the turbulence turnover rate in outdoor environments without the ability to produce large-scale turbulence effects [10–17]. A few benefits of RB tanks are the approach yields conditions that closely resemble real-world laser light propagation through random media along with introducing a more complex scenario of natural convection, which is ubiquitous in both atmospheres and oceans.

Another laboratory method is the generation of atmospheric or underwater optical turbulence using phase screens displayed on spatial light modulators [18,19] or diffractive optical elements [20]. This method of turbulence generation, compared to test tanks, produces highly controllable conditions with optical phase shifts created from known refractive index statistics allowing for direct comparison with theoretical or

numerical approaches. Another benefit is the possibility of changing the propagation distance compared to an RB tank. However, they are limited to the generation device's aperture size, the generation devices' cycling speeds, and the assumptions of the underlying statistics governing the refractive index, such as isotropy and homogeneity.

One type of laboratory implementation to generate underwater optical turbulence is a water chamber that contains a hot plate and cold plate to create a controlled temperature gradient [14]. This process is known as Rayleigh–Bénard (RB) convection, whose strength can be quantified by the Rayleigh number ( $\text{Ra}$ ), Prandtl number ( $\text{Pr}$ ), and aspect ratio ( $\Gamma$ ) [21]:

$$\text{Ra} = \frac{g\alpha_t \Delta T L^3}{\nu D_T}, \quad \text{Pr} = \frac{\nu}{D_T}, \quad \Gamma = \frac{L}{L_c}, \quad (1)$$

where  $g[\text{ms}^{-2}]$  is the acceleration due to gravity,  $\alpha_t[\text{K}^{-1}]$  is the thermal expansion coefficient of water,  $\Delta T[\text{K}]$  is the temperature difference between the thermal sources,  $L_c[\text{m}]$  is characteristic length or height of the chamber,  $L$  is the length of the chamber,  $\nu = \mu/\rho [\text{m}^2\text{s}^{-1}]$  is the kinematic viscosity of water,  $D_T [\text{m}^2\text{s}^{-1}]$  is the thermal diffusivity of water,  $\mu$  is the dynamic viscosity of water, and  $\rho$  is the fluid density of water.

When the Rayleigh number reaches a critical value, which depends on the system's geometry, the boundary layers detach, creating thermal plumes [22]. As the Rayleigh number increases, the effect of gravity creates a buoyancy-driven flow that becomes increasingly turbulent. Within the center region of the tank, away from the thermal boundaries, a mixed region containing quasi-isotropic turbulent trends can form [23]. However, the temperature distribution becomes an active field in buoyancy-driven flow compared with most optical turbulence scenarios where temperature is assumed to be a scalar field [24]. This makes the results in this work a valuable insight into how turbulence containing an active temperature field behaves.

The RB process is a simplified scenario to observe the properties of convective heat and mass transfer that provides insight into many systems containing turbulent thermal convection [23,25–27]. Numerical models of an RB system that employ the Boussinesq approximation, to simplify the Navier–Stokes equations, are sensitive to boundary conditions [28,29]. Although the problem is deterministic, small changes in boundary conditions lead to chaotic RB flow; therefore, the thermal process can be modeled as a random variable [30–32] similar to optical turbulence. This study will focus on using the optical intensity of a laser beam after traversing RB convection to quantify the randomness of the underlying process.

The process of RB convection will be interrogated by measuring the pupil and focal plane intensity fluctuations of a Gaussian laser beam directly after traveling through a water tank producing RB convection [see Fig. 1(a)]. Data will be collected at each optical plane at different Rayleigh numbers by changing the temperature gradient between the plates of the water tank. Calculations of the temporal on-axis intensity and scintillation are made at the pupil and focal plane, along with measurements of the angle of arrival fluctuations at the focal plane. The time series results of each metric are quantified to determine if the process is random and if the change in temperature gradient results in observable trends.

The results of this work contain an additional experimental analysis using pupil and focal plane intensity distributions compared to previous RB tank studies that focused on using beam wander of a small Gaussian beam [11], wavefront sensor techniques [13,14], LED arrays [12], or temperature and velocity measurements [33]. Previous work also used pupil plane intensity statistics [14]; however, the intensity fluctuation distributions were not quantified, focal plane measurements were not taken, and a sweep of the temperature gradient was not performed. This paper will be structured where Section 2 will introduce the necessary theoretical background of the study and Section 3 will discuss the experimental methods. Section 4 presents results determining the type of random process generated by RB convection, and Section 5 presents the statistics of optical parameters in the pupil and focal planes using classical methods, followed by concluding remarks in Section 6.

## 2. THEORETICAL FRAMEWORK

The theory presented here begins with the introduction of the refractive index structure constant,  $C_n^2 [\text{m}^{-2/3}]$ , to the strength of the optical turbulence since this is experimentally measured. Turbulent statistics such as mean intensity and variance are derived from the second and fourth order moments of the laser beam's spatial electric field profile, respectively [5]. The turbulence is assumed isotropic, homogeneous, stationary, and uniform across the propagation distance,  $L$ , to obtain closed form analytic expressions of different beam statistics. Under these assumptions, the Kolmogorov power spectrum of the refractive index fluctuations follows [5]

$$\Phi_n(\kappa) = 0.033 C_n^2 \kappa^{-11/3}, \quad (2)$$

where  $\kappa = (\kappa_x^2 + \kappa_y^2)^{1/2}$  is the spatial wave number. This power spectrum is valid within the inertial-subrange where the scale sizes follow  $1/l_0 \ll \kappa \ll 1/L_0$ , where  $l_0$  is the smallest eddy present, called the inner scale, and  $L_0$  is the largest eddy present, called the outer scale. This region is where large turbulent structures, that inject kinetic energy, break down into smaller structures until dissipated by viscosity. The von Kármán spectrum is a more comprehensive model that includes the effects of inner and outer scale from Eq. (2) defined as [5]

$$\Phi_n(\kappa) = 0.033 C_n^2 \exp[-(\kappa/\kappa_m)^2] (\kappa^2 + \kappa_0^2)^{-11/6}, \quad (3)$$

where  $\kappa_m = 5.92/l_0$  and  $\kappa_0 = 2\pi/L_0$ .

The strength of the turbulence is determined by  $C_n^2$  and is related to the thermal fluctuations [11]

$$C_n^2 = \left( \frac{dn}{dT} \right)^2 C_T^2, \quad (4)$$

and the temperature structure constant,  $C_T^2 [\text{k}^2\text{m}^{-2/3}]$ , is defined as

$$C_T^2 = 0.9\Gamma(1/3)\beta\chi_T\epsilon^{-1/3}, \quad (5)$$

where  $dn/dT = -1.08 \times 10^{-4} \text{ K}^{-1}$  is the mean change of refractive index as a function of water at 632.8 nm [34],  $\Gamma$  is the gamma function, and  $\beta = 0.72$  is the Obukhov–Corrsin constant [35]. The parameters  $\chi_T$  and  $\epsilon$  are general parameters

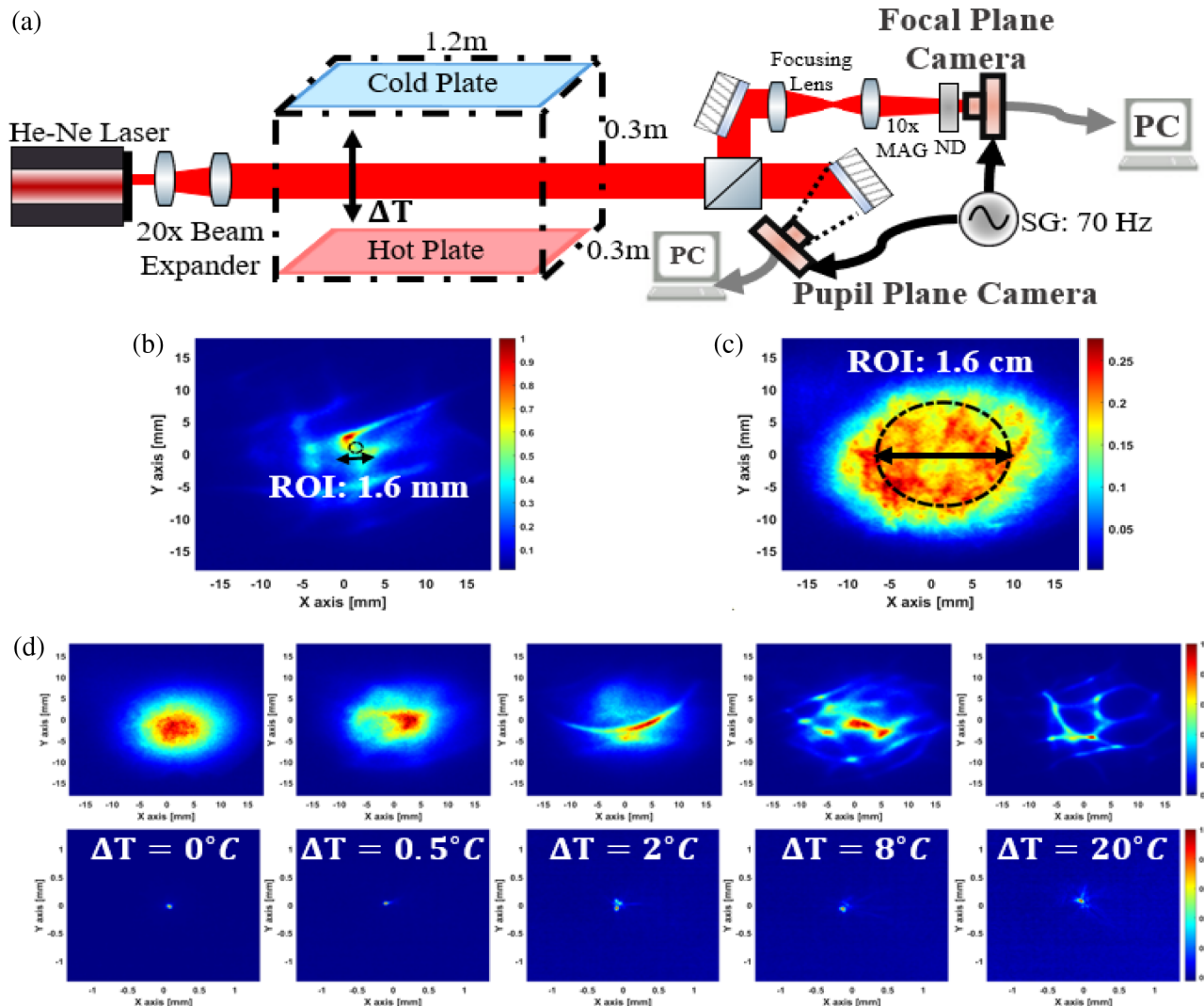


**Fig. 1.** (a) Experimental setup to simultaneously measure the Gaussian beam phase, intensity, and angle of arrival fluctuations. Abbreviations are as follows: neutral density filter (ND), magnification (MAG), and signal generator (SG). (b) Image of the intensity for the case  $\Delta T = 8^\circ C$  with the location of the on-axis region of interest for data processing. (c) Image of the scintillation for the case  $\Delta T = 8^\circ C$  with the location of the on-axis region of interest for data processing. (d) Single images of the pupil plane (top row) and focal plane (bottom row) intensity patterns at different temperature gradients.

of the turbulent flow that are connected to the fluid properties present, namely the thermal diffusivity and kinematic viscosity, respectively.

Equation (6), even in its preliminary form, is compared to experimental data in Section 5 where we show a reasonable agreement to the experimental trend of  $C_n^2$  as a function of temperature gradient for both pupil and focal plane measurements. Equation (6) predicts a scaling law of  $C_T^2$  as a function of the input heat flux for an RB chamber system that can be related to  $C_n^2$  as [36]

$$C_n^2 = \gamma \left( \frac{dn}{dT} \right)^2 \left( \frac{Q}{\rho c_p L_c} \right)^{4/3} (\alpha_t g)^{-2/3}, \quad (6)$$

where  $c_p$  [J/kgK] is the heat capacity of water,  $Q = k \Delta T / L_c$ ,  $k$  [W/mK] is the thermal conductivity of water, and  $\gamma$  is a proportionality constant determined by simulation or experiment

[36]. This equation follows from the Kolmogorov assumptions that the energy supplied by the turbulence from the largest scales contains an eddy turnover time  $t = L_c / w^*$ , where  $w^* = [\alpha_t g L_c Q / c_p \rho]^{1/3}$  is the convective velocity [37].

An inertial-subrange is ubiquitous for any fluid; however, the range of length scales it occurs over can change due to inherent fluid properties. Within RB flow, especially at low Rayleigh number, there is not a well-developed inertial-subrange due to small amounts of turbulent mixing in the center of the chamber [38]. There are more intricate refractive index power spectra models for turbulence in water that include viscosity effects [39–41]. Such models do not incorporate the limited length scales and geometry due to the RB tank and remain usable as estimates of experimentally measured optical quantities. Therefore, Eqs. (4) and (6), that are derived from the assumptions of isotropic, uniform, and homogeneous turbulence, can only be used as estimates and not absolute measurements

of optical parameters. The optical intensity statistics used throughout the experiment to quantify the pupil and focal plane intensity fluctuations will now be defined.

### A. Temporal On-Axis Intensity

Time varying turbulence will create temporal intensity fluctuations that can be quantified using a probability distribution. The temporal on-axis intensity is defined by the amount of light that falls within a small pinhole at the center of the beam's spatial intensity distribution  $I(x, y, t)$  defined as

$$\tilde{I}(t) = \frac{I_p(t)}{\langle I_p(t) \rangle} = \frac{\iint I(x, y, t) A(x, y) dx dy}{\langle \iint I(x, y, t) A(x, y) dx dy \rangle}, \quad (7)$$

where  $A(x, y)$  is a circular pinhole mask with a diameter of 1.6 mm applied to the center of the spatial intensity beam image in post-processing. The intensity collected by the pinhole,  $I_p(t)$ , is normalized by the mean,  $\langle I_p(t) \rangle$ , such that the shape of the intensity fluctuation distribution can be compared at different temperature gradients. The region of interest is chosen to mimic the effects of a small detector to minimize the effects of aperture averaging shown in Fig. 1(b).

### B. Scintillation

Each portion of the beam, recorded as a pixel, has an associated variance of the intensity fluctuations at the end of each time series. The normalized intensity variance is called the scintillation index, defined as [41]

$$\sigma_I^2(x, y) = \frac{\langle I^2(x, y) \rangle - \langle I(x, y) \rangle^2}{\langle I(x, y) \rangle^2} = \frac{\langle I^2(x, y) \rangle}{\langle I(x, y) \rangle^2} - 1. \quad (8)$$

The time dependence is removed because the scintillation index is an averaged parameter calculated using the entire pupil and focal plane intensity time series. Calculation of the scintillation distributions is done within a 1.6 cm circular window placed at the center of the beam shown in Fig. 1(c).

The scintillation index for a plane wave is defined as the Rytov number [Eq. (9)] and denotes different regimes of the optical turbulence strength [5]:

$$\sigma_R^2 = 1.23 C_n^2 k^{7/6} L^{11/6}, \quad (9)$$

where  $k = 2\pi n_0/\lambda$ ,  $\lambda$  is the optical wavelength, and  $n_0$  is the mean refractive index of the medium. A weak turbulence regime can be defined typically when  $\sigma_R^2 < 0.1$  and strong when  $\sigma_R^2 > 1$  with an intermediate regime between the weak and strong cases [5].

The scintillation across a Gaussian beam profile depends on the beam size where scintillation at the beam edges is typically greater than the on-axis scintillation [5]. The processing methods used in this work focus on scintillation within the center of the beam that approximates a plane wave. The region of interest used for data processing calculations is shown in Fig. 1(c).

### C. Angle of Arrival Fluctuations

At the focal plane of a lens, the mean phase variance across the beam wavefront equates to a shift in focal spot location. The

variance of the focal spot movement is known as rms image jitter, which is related to the angle of arrival fluctuations. The angle of arrival fluctuations for a plane wave in turbulence containing refractive index fluctuations described by Eq. (3) are [5]

$$\langle \beta^2 \rangle = 2.91 C_n^2 L (2w_0)^{-1/3} [1 - 0.81(2\kappa_0 w_0)^{1/3}], \quad (10)$$

where  $w_0$  is the  $1/e^2$  beam waist and  $L$  is the outer scale taken to be the characteristic length of the tank [11]. The angle of arrival fluctuations are related to the focal plane displacement  $r_c$  of the optical system with focal length,  $f$ , by [5]

$$r_c = f(\langle \beta^2 \rangle)^{1/2}. \quad (11)$$

### 3. EXPERIMENTAL METHODS

The water tank used in this study was built by the Naval Research Laboratory in Washington, DC, and transferred to the United States Naval Academy, where experiments were performed. The experimental setup in Fig. 1(a) contains RB tank dimensions of 1.2 m  $\times$  0.3 m  $\times$  0.3 m with  $\Gamma = 4$  [14,42,43]. The RB process is created by flat stainless steel immersion plates that heat and chill the bottom and top of the tank to hold fixed temperatures, resulting in close to identical heating and chilling profiles.

The optical transmitter is a HeNe laser at 632.8 nm, with an initial beam size of 1 mm, that is expanded and collimated before entering the RB tank with a beam diameter of 2.1 cm. The expanded beam size is limited to ensure that the beam does not miss the 50 mm diameter optical windows on the entrance and exit of the RB tank. Upon exiting the tank, measurements of the beam are taken in the pupil and focal plane using high-speed cameras. Each high-speed camera is a Fastec IL5 with 5  $\mu\text{m}$  pixel pitch with reference images provided in the first column of Fig. 1(d). The pupil plane intensity is measured after a 50:50 beamsplitter by illuminating a backstop, which is then imaged with a high-speed camera synced to a signal generator with an effective pixel pitch of 80  $\mu\text{m}$ . The focal plane measurements are made with the light from the second port of the beam-splitter with a neutral density filter to reduce camera saturation. The light is focused by a 125 mm focal length lens whose focus is then magnified 10 $\times$  by a second 75 mm focal length lens. This technique is used to increase the footprint of the focal spot on the camera sensor to improve the resolution to obtain more fully resolved intensity and scintillation results. The effective focal length of the two-lens system is 79.8 mm.

A systematic study of the pupil and focal plane intensity statistics is done by varying the temperature gradient between the top and bottom plates. Upon setting a new  $\Delta T$ , the tank is left to stabilize for 15 min to reduce the dynamic effects of changing the temperature gradient. During the measurement time the Prandtl number of the tank ( $\text{Pr} = 6.9$ ) is assumed to be held constant by the mean water temperature. Optical statistics are recorded in 5 min windows at each successive temperature gradient. Each high-speed camera is triggered with a signal generator at 70 Hz to obtain synchronous images.

**Table 1.** Results of  $p$ -Value of  $\chi^2$  Goodness of Fit Tests for Various Distribution Models for the Temporal On-Axis Intensity Fluctuations as a Function of  $\Delta T$

Distributions	$\Delta T^\circ\text{C}$					
	0.5	1	2	3	8	20
Log-normal	0.58	0.00	0.01	0.00	0.00	0.00
Weibull	0.00	0.00	0.00	0.00	0.00	0.00
Gamma	0.56	0.11	0.03	0.03	0.09	0.00
Gamma-gamma	0.74	0.00	0.07	0.41	0.08	0.01
Rician	0.02	0.00	0.00	0.00	0.00	0.00

#### 4. EVALUATION OF PUPIL PLANE RANDOMNESS CREATED IN THE RB TANK

The intensity fluctuations at the pupil plane are the most straightforward metric to determine the randomness of the RB process. The measurements of intensity profile occur at the pupil plane in Fig. 1(a), which is the entrance to the optical system directly after the exit to the RB tank. Normalized histograms of the temporal on-axis intensity fluctuations, using Eq. (7), are compared to known statistical distributions. To test what statistical distributions best fit the data, the  $\chi^2$  goodness of fit is used. First, the normalized histograms of  $\tilde{I}(t)$  are created and fit to various statistical distributions, notably log-normal, Weibull, gamma, Rician, and gamma-gamma. The  $p$ -value of  $\chi^2$  to assume statistical significance of the fit is taken to be 0.05. The  $p$ -value of each distribution fit for different values of the temperature gradient is tabulated in Table 1. Low  $p$ -values are reported due to values of the experimental distribution fluctuating about the best theoretical fit.

A few of these distributions such as the log-normal, gamma-gamma, and Rician have been shown to model atmospheric optical turbulence intensity fluctuations [5,6,44] along with other modifications [45,46]. Intensity fluctuations through water have similar measured models [2] as the atmosphere and others such as the Weibull distribution [47] along with other modifications [48–50].

For four temperature gradients shown in Fig. 2, four distributions are overlapped with the normalized histogram for visual inspection. The distributions chosen are gamma-gamma, Weibull, gamma, and log-normal to showcase the diversity of the fit. As the temperature gradient increases, the width of the intensity distributions increases, creating a longer tail favoring higher fluctuations above the mean, which could indicate a “strong” turbulence regime. The data is best represented by the log-normal, gamma, and gamma-gamma at high temperature, which is the strongest indication that the RB tank generates a random process. This marks the RB tank as an acceptable testbed for studying the impact of optical turbulence on light, such as structured light, non-classical beams, etc. The change in distribution shape can be magnified by plotting the distributions at different values of the temperature gradient on a log-log plot in Fig. 4(a).

The temporal on-axis intensity fluctuations,  $\tilde{I}(t)$ , within a small temperature gradient are generally accepted to follow log-normal statistics [6,44,51]. A log-normal distribution occurs with the assumption that the underlying thermal fluctuations of the system are normally distributed. Within the center of the

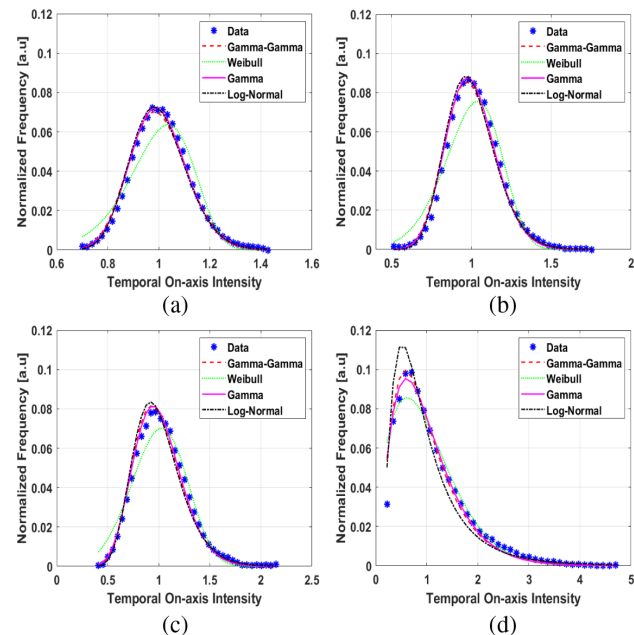


**Fig. 2.** Distributions of the normalized on-axis temporal intensity fluctuations with selected fits for different temperature gradients of (a)  $\Delta T = 0.5^\circ\text{C}$ , (b)  $\Delta T = 2^\circ\text{C}$ , (c)  $\Delta T = 3^\circ\text{C}$ , and (d)  $\Delta T = 20^\circ\text{C}$ .

**Table 2.** Results of the Hurst and Lyapunov Exponents for the Pupil Plane Temporal On-Axis Intensity Fluctuations as a Function of  $\Delta T$

$\Delta T^\circ\text{C}$	0.5	1	2	3	8	20
Hurst	0.78	0.70	0.65	0.62	0.62	0.60
Lyap-Exp	13.20	14.46	18.94	18.06	10.02	2.94

RB tank, the intensity distributions deviate from log-normality possibly due to thermal plumes that reach the center of the tank inducing different fluctuation distributions of the temperature [52]. Wang *et al.* proposed histograms of thermal fluctuations in RB flow where small-scale fluctuations were Gaussian distributed and non-uniform thermal plumes contained an exponential distribution [53]. The gamma-gamma distribution fits well with the measured intensity fluctuation histograms for various temperature gradients. This could be a subject of further experimental and theoretical study.

A second set of statistical tests is run using the Hurst and Lyapunov exponent to determine the randomness of the pupil plane temporal on-axis intensity. The Hurst exponent is a metric of the overall memory of a time series that provides insight to trends in correlation. A random time series contains a Hurst exponent of 0.5, whereas a value greater than 0.5 has a strong long-term trend with positive correlation. The inverse case is when the Hurst exponent is less than 0.5 that indicates a reverse trend or negative correlation [54]. A positive value of Lyapunov exponent can determine if the system is chaotic, in this case randomness [55].

Results of both the Hurst and Lyapunov exponents are shown in Table 2, where for each temperature difference the Hurst value falls between 0.5 and 1, indicating the presence of a random process with temporal correlations on the time scale of measurement. Also, the Lyapunov exponent remains

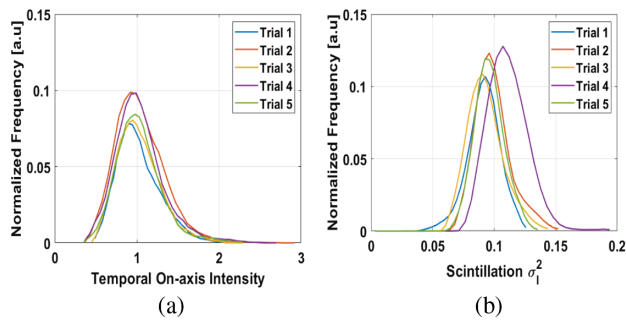


**Fig. 3.** Normalized histograms of (a) pupil plane temporal on-axis intensity and (b) scintillation calculated in the region of interest for five different data trials.

**Table 3. Pupil Plane Temporal On-Axis Intensity Mean (Column 1) and Standard Deviation (Column 2) and Scintillation Mean (Column 3) and Standard Deviation (Column 4) within the Region of Interest for Five Trials of Measurement Where  $\Delta T = 3^\circ\text{C}$**

Trial	$\langle \tilde{I}(t) \rangle$	STDEV $\tilde{I}(t)$	$\langle \sigma_I^2 \rangle$	STDEV $\sigma_I^2$
1	1.02	0.26	0.094	0.010
2	1.03	0.27	0.091	0.014
3	1.02	0.25	0.108	0.015
4	1.03	0.26	0.095	0.011
5	1.03	0.28	0.092	0.013

positive for each case of temporal intensity time series indicating randomness.

#### A. Confirmation of the RB Tank Controllability

To demonstrate the repeatability of the RB tank conditions, five 5-min trials of the pupil plane temporal on-axis intensity fluctuations are obtained at  $\Delta T = 3^\circ\text{C}$ . The pupil plane normalized temporal on-axis intensity fluctuation histograms for the five trials are shown in Fig. 3(a) along with values of the mean ( $\langle \tilde{I}(t) \rangle$ ) and standard deviation (STDEV  $\tilde{I}(t)$ ) in columns two and three of Table 3. The pupil plane on-axis intensity fluctuations for each of the trials follow similar standard deviations showing good repeatability shown in Table 3 and Figs. 3(a) and 3(b).

The normalized pupil plane scintillation histograms [calculated in the region of interest in Fig. 1(c)] are shown in Fig. 3(b) with calculations of the mean ( $\langle \sigma_I^2 \rangle$ ) and standard deviation (STDEV  $\sigma_I^2$ ) in columns four and five in Table 3. Over the range of temperature gradients, based on the mean value of the pupil temporal on-axis intensity and pupil on-axis scintillation, we show that we can control repeatable conditions of optical turbulence.

## 5. STATISTICS OF OPTICAL PARAMETERS

Having shown that the RB tank generates random conditions through analysis of the normalized pupil plane on-axis intensity fluctuations, the optical turbulence parameters can now be investigated. The statistics and  $C_n^2$  of the pupil plane (Section 5.A) and focal plane (Section 5.B) temporal on-axis

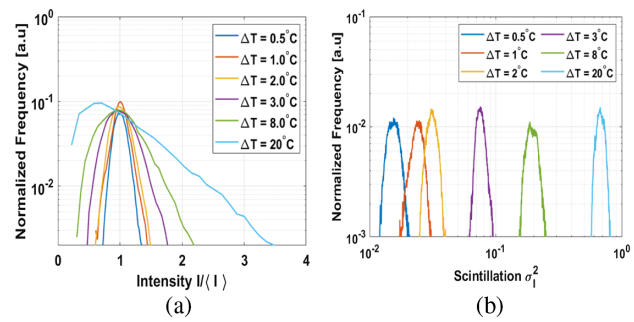


**Fig. 4.** Histograms of pupil plane (a) intensity fluctuations and (b) scintillation for different  $\Delta T$ .

**Table 4. Calculations of the First Four Moments of the Temporal On-Axis Intensity Fluctuation Time Series from Pupil Plane Intensity Distributions in Fig. 4(a) for Varying  $\Delta T$**

$\Delta T(\text{ }^\circ\text{C})$	Mean	STDEV	Skew	Kurtosis
0.5	1.01	0.11	0.77	-0.93
1	1.01	0.13	1.50	1.13
2	1.02	0.15	1.04	-0.50
3	1.02	0.24	0.85	-0.80
8	1.03	0.36	0.92	-0.55
20	1.06	0.67	1.28	0.311

intensity fluctuations are presented followed by comparison of the  $C_n^2$  estimates to Eq. (6) (Section 5.C). Using the theory outlined in Section 2, estimates of  $C_n^2$  can be obtained and compared independently using the pupil plane and focal plane statistics.

#### A. Pupil Plane Statistics

The first four statistical moments (mean, standard deviation, skew, and excess kurtosis) of the pupil plane temporal on-axis intensity distributions shown in Fig. 4(a) are tabulated in Table 4 for the range of temperature differences. We observed that the standard deviation of the pupil plane temporal on-axis intensity distribution increases as temperature increases whereas skew and excess kurtosis fluctuate.

At each temperature gradient, the spread of the fluctuations increases where the most noticeable differences are for the cases  $\Delta T = 8^\circ\text{C}$  and  $20^\circ\text{C}$  [see Fig. 4(a)]. We observe that the positive skew of the pupil plane temporal on-axis intensity distributions increases as the gradient temperature gradient increases. The distribution also contains a constant positive skew that increases with turbulence strength.

The scintillation distribution calculated in the region of interest for increasing temperature gradient is shown in Fig. 4(b). By visual inspection, the distributions contain a similar width and shape, but different mean values shown in Table 5. The results in Table 5 for the scintillation contain similar results to Table 4. This indicates that the intensity fluctuations and scintillation have similar trends and an overall increase in optical turbulence strength as the temperature gradient increases. Table 6 summarizes the estimates of  $C_n^2$  using the pupil plane statistics. Estimates of  $C_n^2$  are obtained using the mean scintillation of the

**Table 5.** Summary of Various Scintillation Statistics Derived from Pupil Plane 2D Scintillation Distribution for Varying  $\Delta T$

$\Delta T(^{\circ}\text{C})$	Mean	STDEV	Skew	Kurtosis
0.5	0.016	0.002	1.65	1.20
1	0.024	0.003	1.63	1.28
2	0.032	0.003	1.91	2.27
3	0.077	0.008	2.10	3.10
8	0.20	0.02	1.46	0.57
20	0.68	0.054	1.91	2.188

**Table 6.** Summary of the Rayleigh Number and  $C_n^2$  Estimates Derived from Pupil Plane Intensity Fluctuations for Varying  $\Delta T$

$\Delta T(^{\circ}\text{C})$	$\text{Ra} \times 10^8$	$\sigma_R^2$	$C_n^2 \times 10^{-10} [\text{m}^{-2/3}]$
0.5	2.5	0.016	0.64
1	5.0	0.024	0.96
2	1.0	0.032	1.28
3	1.5	0.077	3.08
8	4.0	0.20	7.99
20	10.0	0.68	27.19

distributions in Fig. 4(b) and values in Table 5 upon substitution into Eq. (9). As  $\Delta T$  increases, the most significant change of statistics occurs for the smaller temperature gradients. More detail on this result will be given in Section 5.C.

## B. Focal Plane Statistics

The statistics in the focal plane are calculated similar to the statistics in the pupil plane. Due to the smaller region of illumination on the camera, the region of interest created for the on-axis intensity [calculated in Eq. (7)] and scintillation is reduced in size. Both the temporal on-axis intensity and scintillation histograms are computed along with the angle of arrival fluctuations.

### 1. Intensity Fluctuation Results

The temporal on-axis intensity fluctuations of the focal plane are illustrated in Fig. 5(a). We observe that for higher temperature gradients ( $\Delta T = 3^{\circ}\text{C}$ ,  $8^{\circ}\text{C}$ , and  $20^{\circ}\text{C}$ ), the intensity distribution overlaps and spreads out compared to the lower cases of the temperature gradient ( $\Delta T = 0.5^{\circ}\text{C}$ ,  $1^{\circ}\text{C}$ , and  $2^{\circ}\text{C}$ ). Further investigation into this behavior is necessary.

For the focal plane measurements, the standard deviation of the intensity fluctuations did not exhibit a significant trend across any of the distribution statistical moments shown in Table 7.

The scintillation distributions measured in the focal plane show different trends compared to those of the pupil plane. The mean scintillation of each distribution as a function of temperature gradient, shown in Fig. 5(b), does not show an increasing trend like the pupil plane distributions in Fig. 4(b). This is elaborated by the tabulated values of the mean focal plane scintillation in Table 8.

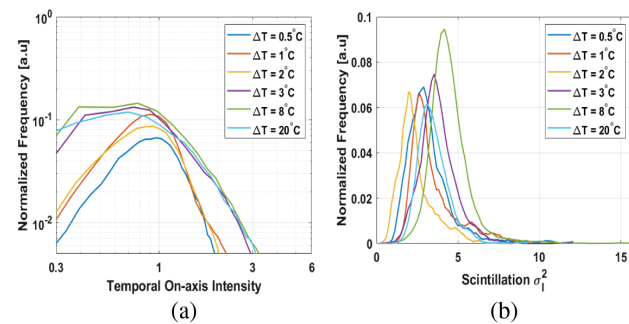


**Fig. 5.** (a) Histogram of focal plane temporal on-axis intensity fluctuations for different  $\Delta T$ . (b) Histograms of focal plane scintillation for different  $\Delta T$ .

**Table 7.** Summary of Various Intensity Statistics Derived from Focal Plane Intensity Fluctuations for Varying  $\Delta T$

$\Delta T(^{\circ}\text{C})$	Mean	STDEV	Skew	Kurtosis
0.5	1.04	0.38	1.23	0.09
1	1.06	0.52	2.31	4.16
2	1.05	0.52	1.73	1.67
3	1.12	0.80	2.75	6.56
8	1.14	1.01	3.21	10.14
20	1.12	0.87	2.42	5.01

**Table 8.** Summary of Various Scintillation Statistics Derived from Focal Plane Intensity Fluctuation Distribution for Varying  $\Delta T$

$\Delta T(^{\circ}\text{C})$	Mean	STDEV	Skew	Kurtosis
0.5	3.24	1.47	1.74	4.86
1	3.50	1.45	1.84	5.42
2	2.41	1.09	1.85	5.86
3	3.77	1.11	1.80	5.22
8	4.45	1.23	2.25	6.94
20	3.50	0.95	1.41	3.58

### 2. Angle of Arrival Results

The angle of arrival fluctuations are measurements of the focal spot jitter, illustrated in Fig. 6(a), at the focus of a lens for the case  $\Delta T = 2^{\circ}\text{C}$ . The color bar represents the start of the 5 min measurement (blue) and the end of the measurement (red). In contrast, Fig. 6(b) shows the focal spot jitter for the  $\Delta T = 20^{\circ}\text{C}$  where the region of focal spot wander increases. In both cases, the jitter centers around the main axis of the beam with no preferred direction in the region of interest. Figures 6(c) and 6(d) show the normalized histograms of the focal spot jitter in the  $x$  and  $y$  directions, respectively. At each  $\Delta T$ , the distributions of the focal spot centroids in the  $x$  and  $y$  directions are Gaussian distributed by visual inspection.

Determination of the angle of arrival fluctuations is done by using the time series of the  $x(t)$  and  $y(t)$  focal plane jitter to calculate the radial fluctuations  $r(t)^2 = x(t)^2 + y(t)^2$ . Then the variance of  $r(t)$  is found to be the angle of arrival fluctuations ( $\langle \beta^2 \rangle$ ) from Eq. (11). The results are summarized in Table 9. Due to the fact that the scintillation fluctuations are not varying, a constant value of  $C_n^2$  is calculated. A possible explanation of

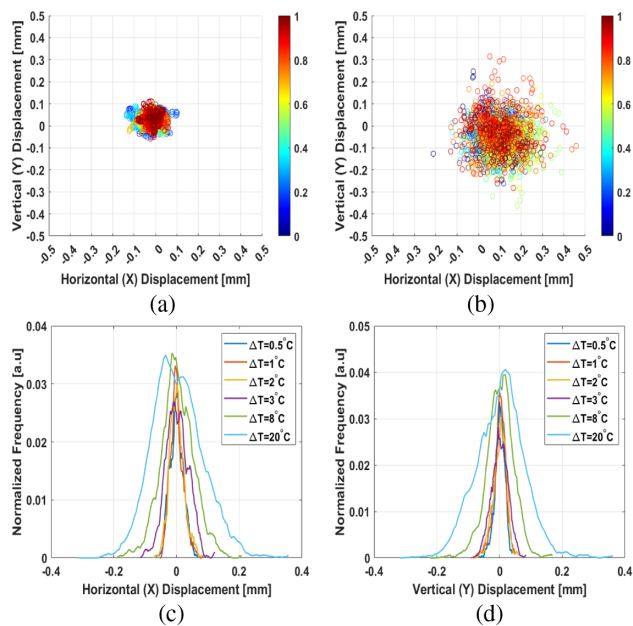


**Fig. 6.** Example of the focal plane angle of arrival histograms and the spot movement as a function of temperature gradient and time.

**Table 9. Summary of the Rytov Number, Angle of Arrival (AoA) Fluctuations, and  $C_n^2$  Estimates from Focal Plane Intensity Fluctuations for Varying  $\Delta T$**

$\Delta T$ (°C)	$\sigma_R^2$	$C_n^2$ [ $m^{-2/3}$ ] $\times 10^{-10}$ (Scin)	$C_n^2$ [ $m^{-2/3}$ ] $\times 10^{-10}$ (AoA)
0.5	0.72	28.79	0.22
1	0.73	29.19	0.82
2	0.70	27.99	1.73
3	0.57	22.79	3.23
8	0.47	18.79	9.08
20	0.11	4.40	48.39

such behavior is that the resolution of the camera sensor cannot capture the small deviations and small features within the focal plane intensity distribution. The angle of arrival estimate for  $C_n^2$  increases as a function of temperature gradient conversely with the focal plane scintillation that begins to saturate. Therefore, the angle of arrival is a better method to estimate  $C_n^2$  using focal plane measurements.

### C. Comparison of $C_n^2$ Measurements in the Focal and Pupil Planes

Using the trends observed in both the pupil and focal planes, comparisons of  $C_n^2$  can be made using the pupil plane scintillation and focal plane angle of arrival fluctuations as a function of the temperature gradient in Eq. (6). Figure 7 shows the curve of best fit using Eq. (6) where  $\gamma$  is determined to be  $2.2 \times 10^{-5}$  for the pupil plane estimates (red) and  $6.9 \times 10^{-5}$  for the angle of arrival estimates (green). The scaling law  $C_T^2 \sim \Delta T^{4/3}$  predicted by Handler [36] appears to follow the increase of  $C_n^2$  as a function of the temperature gradient. However, there is a discrepancy of the  $C_n^2$  estimates not agreeing from the pupil plane scintillation and focal plane angle of arrival fluctuations. This can be attributed to the number of assumptions placed on

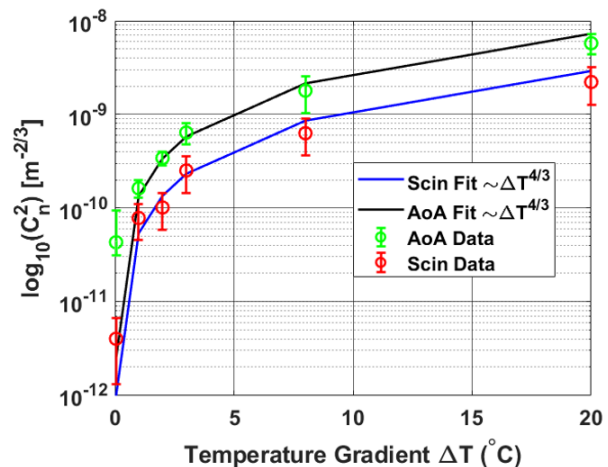


**Fig. 7.** Estimates of  $C_n^2$  versus  $\Delta T$  for scintillation and angle of arrival fluctuations compared with Eq. (6) as theory.

the refractive index power spectrum to derive Eqs. (9) and (10), which are not derived for RB turbulence conditions.

## 6. CONCLUSIONS

Within this study, the characteristics of RB convection were estimated by synchronous optical intensity measurements in the pupil plane and focal plane for different temperature gradients. The experimental data was analyzed using several statistical methods to show that the underlying random process is temporally correlated (by Hurst exponent), chaotic (by Lyapunov exponent), and statistically repeatable (see Section 6.A). We found a good match between the pupil plane temporal on-axis intensity fluctuations and the gamma-gamma and log-normal probability density functions to demonstrate the randomness of the process created by RB convection. These results validate the RB process as suitable for light propagation studies through random media. The applications include sensing, communications, imaging, and structured light and non-classical beam propagation. Pupil plane intensity distributions showed a change in standard deviation, whereas focal plane intensity distributions did not show significant trends in statistical moments as a function of the temperature gradient. Both pupil and focal plane statistics observed no significant change in distribution shape.

Estimates of  $C_n^2$  using pupil plane scintillation and focal plane angle of arrival fluctuations did not produce the same value; however, their order of magnitude and predicted trend as a function of temperature gradient were similar (see Fig. 7). This insight provides strong evidence that the underlying turbulence contains coherent structures, such as thermal plumes, not predicted under the assumptions of Kolmogorov turbulence.

### A. Future Work

The RB flow is inherently produced by buoyancy, which is neglected in these optical theories of turbulence using the assumption of isotropic and homogeneous statistics. Due to the heating profile along the beam path using uniformly heated plates, the uniformity of the turbulence along the propagation

path is created by turbulent structures rather than the heating profile. This effect is partly due to the temperature field becoming an active field compared, which is not assumed in optical turbulence models that assume the temperature field is a scalar quantity [56]. This effect produces many questions about how RB convection at a lab scale can be extrapolated to larger-scale buoyancy-driven flow or stratification of boundary layers within the atmosphere or ocean and will be the subject of upcoming studies.

Further analytic study of different intensity fluctuation distribution models can be explored for different temperature gradients to strengthen the claim that the RB process is random and can be used to test the performance of light propagation through natural convection. This theoretical study can also be followed up by further analytic methods to address how optical turbulence behaves in the presence of an active field. Additionally, since the pupil and focal plane measurements are taken simultaneously, the underlying turbulence structure could be revealed using non-classical data processing methods such as machine learning.

**Funding.** Office of the Secretary of Defense (SMART SEED Grant).

**Acknowledgment.** Thank you to Dr. Stephen Wiggins of the USNA for extensive and insightful conversations and to the reviewers for their time and excellent comments to improve the manuscript.

**Disclosures.** The authors declare no conflicts of interest.

**Data availability.** Data available upon request.

## REFERENCES

1. W. Hou, S. Woods, E. Jarosz, et al., "Optical turbulence on underwater image degradation in natural environments," *Appl. Opt.* **51**, 2678–2686 (2012).
2. Y. Baykal, Y. Ata, and M. C. Gökçe, "Underwater turbulence, its effects on optical wireless communication and imaging: a review," *Opt. Laser Technol.* **156**, 108624 (2022).
3. O. Korotkova and J.-R. Yao, "Bi-static LIDAR systems operating in the presence of oceanic turbulence," *Opt. Commun.* **460**, 125119 (2020).
4. M. Kalensky, E. J. Jumper, M. R. Kemnetz, et al., "In-flight measurement of atmospheric-imposed tilt: experimental results and analysis," *Appl. Opt.* **61**, 4874–4882 (2022).
5. L. C. Andrews and R. L. Phillips, *Laser Beam Propagation through Random Media*, 2nd ed. (SPIE, 2005).
6. V. I. Tatarskii, *Effects of the Turbulent Atmosphere on Wave Propagation* (1971).
7. G. Nootz, E. Jarosz, F. R. Dalglish, et al., "Quantification of optical turbulence in the ocean and its effects on beam propagation," *Appl. Opt.* **55**, 8813–8820 (2016).
8. B. N. Iii, S. Lilledahl, J. T. Coffaro, et al., "Deployable scintillometer for ocean optical turbulence characterization," *Proc. SPIE* **11752**, 53–63 (2021).
9. J. A. Anguita, C. Pirela, A. Seguel, et al., "Experimental testbed for the evaluation of optical vortices propagated over 900 meters," in *Optica Advanced Photonics Congress* (Optica Publishing Group, 2022).
10. W. Hou and S. Matt, "EO signal propagation in a simulated underwater turbulence environment," in *OCEANS 2014—TAIPEI* (2014), pp. 1–6.
11. G. Nootz, S. Matt, A. Kanaev, et al., "Experimental and numerical study of underwater beam propagation in a Rayleigh-Bénard turbulence tank," *Appl. Opt.* **56**, 6065–6072 (2017).
12. J. P. Montoya, M. Segel, S. Gladysz, et al., "Measurements of temperature and image motion structure functions in a Rayleigh-Bénard water tank," in *Imaging and Applied Optics 2019 (COSI, IS, MATH, pcAOP)* (Optica Publishing Group, 2019).
13. V. A. Kulikov, M. S. Andreeva, A. V. Koryabin, et al., "Method of estimation of turbulence characteristic scales," *Appl. Opt.* **51**, 8505–8515 (2012).
14. N. A. Ferlic, S. Avramov-Zamurovic, O. O'Malley, et al., "Synchronous optical intensity and phase measurements to characterize Rayleigh-Bénard convection," *J. Opt. Soc. Am. A* **40**, 1662–1672 (2023).
15. J. A. Anguita and J. E. Cisternas, "Influence of turbulence strength on temporal correlation of scintillation," *Opt. Lett.* **36**, 1725–1727 (2011).
16. M. Cox, "The characterization of atmospheric turbulence and its effect on laser beam propagation," all theses (2023).
17. J. P. Wiley, E. Robertson, N. A. Ferlic, et al., "High data-rate communication link supported through the exploitation of optical channels in a characterized turbulent underwater environment," *Opt. Express* **31**, 31839–31852 (2023).
18. J. D. Phillips, M. E. Goda, and J. Schmidt, "Atmospheric turbulence simulation using liquid crystal spatial light modulators," *Proc. SPIE* **5894**, 589406 (2005).
19. L. Burger, I. A. Litvin, and A. Forbes, "Simulating atmospheric turbulence using a phase-only spatial light modulator," *South African J. Sci.* **104**, 129–134 (2008).
20. S. Hippler, F. Hormuth, D. J. Butler, et al., "Atmosphere-like turbulence generation with surface-etched phase-screens," *Opt. Express* **14**, 10139–10148 (2006).
21. S. Grossmann and D. Lohse, "Scaling in thermal convection: a unifying theory," *J. Fluid Mech.* **407**, 27–56 (2000).
22. S. Grossmann and D. Lohse, "Fluctuations in turbulent Rayleigh-Bénard convection: the role of plumes," *Phys. Fluids* **16**, 4462–4472 (2004).
23. D. Lohse and O. Shishkina, "Ultimate turbulent thermal convection," *Phys. Today* **76**, 26–32 (2023).
24. R. J. Hill, "Models of the scalar spectrum for turbulent advection," *J. Fluid Mech.* **88**, 541–562 (1978).
25. A. Bershadskii, *Strong Chaotic Fluctuations of Laser Beams Propagating Through Temperature Inhomogeneities in the Atmosphere* (2020).
26. D. Lohse and K.-Q. Xia, "Small-scale properties of turbulent Rayleigh-Bénard convection," *Annu. Rev. Fluid Mech.* **42**, 335–364 (2010).
27. A. V. Getling, *Rayleigh-Bénard Convection: Structures and Dynamics* (World Scientific, 1998).
28. D. J. Tritton, *Physical Fluid Dynamics*, 2nd ed. (Clarendon, 1988).
29. E. Bodenschatz, W. Pesch, and G. Ahlers, "Recent developments in Rayleigh-Bénard convection," *Annu. Rev. Fluid Mech.* **32**, 709–778 (2000).
30. V. M. Zaitsev and M. I. Shliomis, "Hydrodynamic fluctuations near the convection threshold," *J. Exp. Theor. Phys.* **32**, 866–870 (1971).
31. R. Graham, "Hydrodynamic fluctuations near the convection instability," *Phys. Rev. A* **10**, 1762–1784 (1974).
32. J. Swift and P. C. Hohenberg, "Hydrodynamic fluctuations at the convective instability," *Phys. Rev. A* **15**, 319–328 (1977).
33. S. Matt, W. Hou, W. Goode, et al., "Introducing SiTTE: a controlled laboratory setting to study the impact of turbulent fluctuations on light propagation in the underwater environment," *Opt. Express* **25**, 5662–5683 (2017).
34. X. Quan and E. S. Fry, "Empirical equation for the index of refraction of seawater," *Appl. Opt.* **34**, 3477–3480 (1995).
35. R. J. Hill and S. F. Clifford, "Modified spectrum of atmospheric temperature fluctuations and its application to optical propagation," *J. Opt. Soc. Am. A* **68**, 892–899 (1978).
36. R. A. Handler, R. J. Watkins, S. Matt, et al., *Model for the Structure Function Constant for Index of Refraction Fluctuations in Rayleigh-Bénard Turbulence* (2023).
37. R. J. Adrian, R. T. D. S. Ferreira, and T. Boberg, "Turbulent thermal convection in wide horizontal fluid layers," *Exp. Fluids* **4**, 121–141 (1986).
38. M. Sano, X. Z. Wu, and A. Libchaber, "Turbulence in helium-gas free convection," *Phys. Rev. A* **40**, 6421–6430 (1989).
39. V. V. Nikishov and V. I. Nikishov, "Spectrum of turbulent fluctuations of the sea-water refraction index," *Int. J. Fluid Mech. Res.* **27** (2000).
40. R. J. Hill, "Optical propagation in turbulent water," *J. Opt. Soc. Am.* **68**, 1067–1072 (1978).

41. O. Korotkova, "Light propagation in a turbulent ocean," in *Progress in Optics* (2019), pp. 1–43.
42. S. Avramov-Zamurovic, A. T. Watnik, J. R. Lindle, et al., "Machine learning-aided classification of beams carrying orbital angular momentum propagated in highly turbid water," *J. Opt. Soc. Am. A* **37**, 1662–1672 (2020).
43. W. A. Jarrett, S. Avramov-Zamurovic, J. M. Esposito, et al., "Neural network classification of beams carrying orbital angular momentum after propagating through controlled experimentally generated optical turbulence," *J. Opt. Soc. Am. A* **41**, B1–B13 (2024).
44. G. Parry and P. N. Puaey, "K distributions in atmospheric propagation of laser light," *J. Opt. Soc. Am.* **69**, 796–798 (1979).
45. W. S. Rabinovich, R. Mahon, and M. S. Ferraro, "Estimating maritime free space optical link performance using models based on experimental measurements," *Proc. SPIE* **12691**, 126910A (2023).
46. O. Korotkova, S. Avramov-Zamurovic, R. Malek-Madani, et al., "Probability density function of the intensity of a laser beam propagating in the maritime environment," *Opt. Express* **19**, 20322–20331 (2011).
47. M. P. Bernotas and C. Nelson, "Probability density function analysis for optical turbulence with applications to underwater communications systems," *Proc. SPIE* **9827**, 98270D (2016).
48. H. M. Oubei, E. Zedini, R. T. ElAfandy, et al., "Simple statistical channel model for weak temperature-induced turbulence in underwater wireless optical communication systems," *Opt. Lett.* **42**, 2455–2458 (2017).
49. E. Zedini, H. M. Oubei, A. Kammoun, et al., "Unified statistical channel model for turbulence-induced fading in underwater wireless optical communication systems," *IEEE Trans. Commun.* **67**, 2893–2907 (2019).
50. Y. M. Shishter, R. Young, and F. H. Ali, "Modelling the intensity distribution of underwater optical wave propagation in the presence of turbulence and air bubbles," *Optik* **270**, 170006 (2022).
51. S. F. Clifford and R. J. Hill, "Relation between irradiance and log-amplitude variance for optical scintillation described by the k distribution," *J. Opt. Soc. Am.* **71**, 112–114 (1981).
52. J. Lülf, M. Wilczek, and R. Friedrich, "Temperature statistics in turbulent Rayleigh-Bénard convection," *New J. Phys.* **13**, 015002 (2011).
53. Y. Wang, X. He, and P. Tong, "Turbulent temperature fluctuations in a closed Rayleigh-Bénard convection cell," *J. Fluid Mech.* **874**, 263–284 (2019).
54. A. Clauset, C. R. Shalizi, and M. E. J. Newman, "Power-law distributions in empirical data," *SIAM Rev.* **51**, 661–703 (2009).
55. A. Vulpiani, F. Cecconi, and M. Cencini, *Chaos: From Simple Models to Complex Systems* (World Scientific, 2009).
56. A. Celani, M. Cencini, A. Mazzino, et al., "Active and passive fields face to face," *New J. Phys.* **6**, 72 (2004).